# Metal-Enhanced Hg²⁺-Responsive Fluorescent Nanoprobes: From Morphological Design to Application to Natural Waters

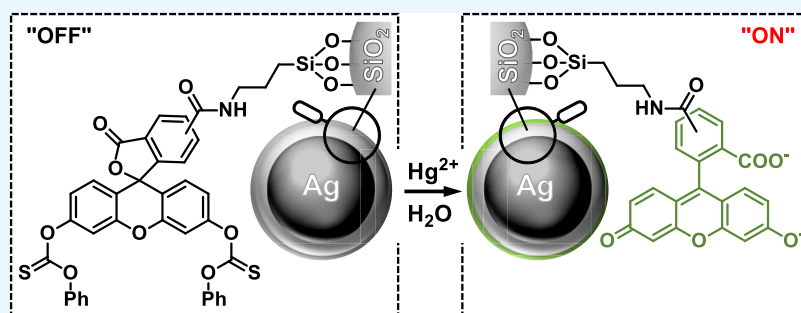Audrey Picard-Lafond, Dominic Larivière, and Denis Boudreau*

ACCESS | 📊 Metrics & More | 📄 Article Recommendations | 🆂🅸 Supporting Information

**ABSTRACT:** Metal-enhanced fluorescence (MEF) is a powerful tool in the design of sensitive chemical sensors by improving brightness and photostability of target-responsive fluorophores. Compounding these advantages with the modest hardware requirements of fluorescence sensing compared to that of centralized elemental analysis instruments, thus expanding the use of MEF to the detection of low-level inorganic pollutants, is a compelling aspiration. Among the latter, monitoring mercury in the environment, where some of its species disseminate through the food chain and, in time, to humans, has elicited a broad research effort toward the development of Hg²⁺-responsive fluorescent sensors. Herein, a Hg²⁺-sensitive MEF-enabled probe was conceived by grafting a Hg²⁺-responsive fluorescein derivative to concentric Ag@SiO₂ NPs, where the metallic core enhances fluorescence emission of molecular probes embedded in a surrounding silica shell. Time-resolved fluorescence measurements showed that the fluorophore's excited-state lifetime decreases from 3.9 ns in a solid, coreless silica sphere to 0.4 ns in the core−shell nanoprobe, granting the dye a better resistance to photobleaching. The Ag-core system showed a sizable improvement in the limit of detection at 2 nM (0.4 ppb) compared to 50 nM (10 ppb) in silica-only colloids, and its effectiveness for natural water analysis was demonstrated. Overall, the reported nanoarchitecture hints at the potential of MEF for heavy metal detection by fluorescence detection.

## 1. INTRODUCTION

Fluorescence is widely used for the development of chemical sensors as it entails simple instrumentation and offers high sensitivity and a versatility granted by the vast choice of accessible dyes with distinct optical properties, whether these molecules are commercially purchased or custom-designed for specific analytes.[1,2] However, fluorescent chemosensors are generally hindered by the intrinsic drawbacks of organic dyes such as collisional quenching, hydrophobicity, and photodegradation under intense irradiation, shortcomings that can become particularly significant when the amount of targets is very low.[3,4] Incorporation of classical fluorophores into nanoparticular supports such as silica allows to overcome some of these faults by providing a denser emitter with higher brightness and increased photostability.[5−7] Silica is also a transparent, chemically inert, and water-soluble template that can be easily conjugated to biomolecules and molecular probes. As a result, a number of silica-based analytical platforms have been reported.[8−10]

A downside to dye-doped silica particles is that their luminosity can be hindered by self-quenching caused by resonant energy transfer at high fluorophore concentrations.[11,12] To mitigate this phenomenon, metal-enhanced fluorescence (MEF) has been employed to limit nonradiative decay from energy transfer by modifying the relaxation pathways of silica-embedded fluorophores.[13,14] Noble metal nanoparticles can support localized surface plasmon resonances (LSPRs) induced by the collective oscillation of conduction electrons upon excitation with light of appropriate frequency, granting them unique optical properties modulated by the particles' composition, size, shape, and nature of

surrounding media.[15] MEF originates from the close-range interaction of a dye molecule with a plasmonic nanoparticle.[16] More precisely, irradiating a plasmonic nanoparticle at its LSPR frequency creates a strong electric field at the surface, and a dye positioned in this field experiences an antenna effect enhancing both excitation and emission pathways. Benefits to the dye's optical properties compared to their free-floating and silica-embedded forms include improved emission intensity, better resistance to photobleaching, and reduced self-quenching through shortened excited-state lifetimes.[13] Numerous photophysical studies and analytical applications of MEF systems have been reported, with morphological features of the particles being key parameters.[17−22] On the one hand, larger nanoparticles offer better scattering efficiency for inducing dipole−dipole interactions with the dyes in proximity. On the other hand, maximum fluorescence enhancement is observed when the dye is positioned at a set distance from the core surface, where plasmon-−dye coupling is still felt while quenching from nonradiative energy transfer is limited.[23]

Among the many MEF-enabled systems described in the literature, fluorescein (Fl) is arguably the most frequently used dye, whether to perform photophysical studies[13,24−32] or to exploit its pH sensitivity for sensing.[33−35] In particular, an extensive structure−property study of Fl-appended silica-coated concentric silver nanoparticles (Ag@SiO$_2$ NPs) conducted by Asselin et al.[26] showed that 75 nm Ag cores coated with a 7-nm-thick SiO$_2$ spacer produced a 10 times enhancement in emission intensity for Fl when immobilized within a 1-nm-thin SiO$_2$ surface layer. These structures were also immobilized onto glass surfaces and incorporated into microfluidic devices to perform real-time pH mapping of live biochemical systems.[33,36] Recently, a review article addressed the relevance of plasmon-enhanced pH nanoprobes and asserted that one of the next junctures in applied research is to expand their use to environmentally relevant analytes,[37] for example, by chemically modifying common dyes such as fluorescein to instigate sensitivity to other inorganic compounds (e.g., hydrogen sulfide,[38] perborate,[39] superoxide[40,41] and peroxide,[42] mercury ions,[43] and many more).[44]

Amidst many environmental contaminants necessitating monitoring, mercury is one that entices comprehensive attention due to its significant distribution in the environment and the high toxicity of its methylated form, methylmercury, that is naturally generated by microbial organisms.[45] The bioaccumulation and biomagnification of methylmercury that ensue in the food chain lead to a significant threat to human health by causing damage to the endocrine, respiratory, and central nervous systems.[46] These hazards can be alleviated, in part, by setting up policies and thoroughly monitoring the contaminant. To this end, the World Health Organization (WHO) recommends a maximum tolerable level of mercury contamination of 1 ppb (5 nM) in drinking water,[47] and mercury monitoring is accomplished by dependable analytical techniques such as atomic absorption−emission spectrometry and inductively coupled mass spectrometry.[48]

In recent years, the interest in real-time and field-deployable Hg sensing has motivated the development of a variety of optical probes offering faster, cheaper, and simpler operation than sophisticated traditional laboratory-based instrumentation.[49−51] These probes are also well-suited to simple and compact instrumentation platforms that are essential to point-of-need use. Therefore, a plethora of emissive molecular dyes have been synthetically modified to induce an alteration of their absorptive and/or emissive properties upon interacting with Hg$^{2+}$.[52−57] As a case in point, a Hg$^{2+}$-sensitive "turn on" molecular probe with an Fl backbone was recently reported, where a nonemissive fluorescein dithionocarbonate incurs a Hg$^{2+}$-assisted hydrolysis leading to the release of Fl emissivity.[43]

A few examples exist in the literature of MEF being used to enhance the response of Hg$^{2+}$-sensitive dye derivatives. Some systems are based on Hg$^{2+}$-sensitive rhodamine spirolactam dyes appended to noble metal nanoparticles dispersed in a mesoporous silica network,[58,59] while others proceed by spiking bare Ag nanoparticles in a solution containing a fluorogenic Hg$^{2+}$ probe.[60,61] However, neither of these approaches capitalize on the strong dependence of MEF on dye−metal distance and nanoparticle size, as was demonstrated in a number of studies involving other fluorescent Ag- and Au-based MEF nanostructures.[26,35,62−65]

In the work presented herein, a MEF-enabled Hg$^{2+}$-sensitive probe combining fluorescein dithionocarbonate (Fl-DTC) moieties and Ag@SiO$_2$ NPs is demonstrated. The core−shell design is based on a nanoparticle geometry (i.e., 70 nm Ag core diameter, 8 nm thick silica shell) previously optimized for fluorescein.[26] Coreless, solid silica nanospheres grafted with Fl-DTC were used as a model colloidal substrate to characterize and validate each synthetic step and to provide a comparative unenhanced structure for photophysical MEF studies using steady-state and time-resolved fluorescence spectroscopy. The analytical performance of the as-prepared silica-based and MEF-enabled nanoparticles toward Hg$^{2+}$ sensing was evaluated, with limits of detection (LODs) of 50 nM (10 ppb) and 2 nM (0.4 ppb), respectively, highlighting the benefits of MEF in colloidal probe design. Finally, testing the nanosensor on river and lake water samples demonstrated its potential for use in the field.

## 2. EXPERIMENTAL SECTION

**2.1. Chemicals and Materials.** Mercury(II) nitrate monohydrate (≥99.99%), sodium borohydride (99.99%), sodium citrate tribasic dihydrate (≥99.0%), 5-(6)-carboxy-fluorescein succinimidyl ester (FAM-SE, ≥80%), o-phenyl chlorothionoformate (PCTF, 99%), dimethylamine (DMA, 40% wt solution in water), triethylamine (≥99.5%), N,N-diisopropylethylamine (DIPEA, 99.5%), anhydrous N,N-dimethylformamide (DMF, 99.8%), N-(2-hydroxyethyl)-piperazine-N′-ethanesulfonic acid (HEPES, 99.5%), (3-amino-propyl) triethoxysilane (APTES, 99%), and anhydrous acetonitrile (99.8%) were purchased from Sigma-Aldrich. Silver nitrate (99.9995%) was obtained from Strem Chemicals. Tetraethyl orthosilicate (TEOS, 99.9%) was purchased from Alfa Aesar. Anhydrous ethanol was purchased from GreenField Global. Ammonium hydroxide solution (28−30% wt NH$_3$) was purchased from Anachemia. Sodium hydroxide was purchased from J.T. Baker. Nanopure water (18 MΩ) was used for all aqueous experiments, and all chemicals were used without further purification.

**2.2. Instrumentation.** High-resolution mass spectra (HRMS) were recorded with an Agilent 6210 time-of-flight (TOF) LC-MS apparatus equipped with an ESI ion source (Agilent Technologies, Canada). Fluorescence spectra were acquired on a Fluorolog 3 spectrofluorimeter (Jobin-Yvon Horiba). For steady-state fluorescence experiments, 5 nm slits and $\lambda_{exc}$ = 485 nm were used. For kinetic-based fluorescence experiments, the following parameters were used: 5 nm slits,

$\lambda_{exc}$ = 485 nm, $\lambda_{em}$ = 520 nm, and $\Delta t$ = 2 s. The acquired raw spectra were corrected for the spectrofluorometer's spectral response function in all experiments. Silver-core nanoparticles were characterized by UV−visible spectrophotometry (Cary 50, Agilent Technologies, Canada) using 10 mm path length quartz cells. Dry size distributions of all nanoparticle samples were determined by transmission electron microscopy (TEM; model JEM-1230, JOEL, Tokyo, Japan) at an accelerating voltage of 80 kV. Samples were prepared by drop casting the particle dispersions on carbon-coated copper grids (200 mesh, Electron Microscopy Sciences, Hatfield, PA) and allowing them to air dry prior to measurements. Image analysis was performed for ≥100 particles per sample using the ImageJ software. Hydrodynamic size distribution and number concentration of all nanoparticle samples were measured by nanoparticle tracking analysis (NTA; NanoSight NS300, Malvern Instruments, Worcestershire, United Kingdom) equipped with a 0.2 mL microfluidic sample chamber, a 488 nm laser module, and an external syringe pump to ensure a continuous flow rate of 20 $\mu$L/min throughout the measurements. The NTA apparatus was calibrated with commercial calibration beads from Bangs Laboratories (Fisher, IN). Replicates were completed by recording four 45 s videos of the eluting samples, and data treatment was performed with the NanoSight NTA software (version 2.3). $\zeta$-Potential was measured by a $\zeta$-potential analyzer ($\zeta$; Zetasizer NanoZS, Malvern Instruments, Worcestershire, United Kingdom). Time-resolved fluorescence measurements were performed by time-correlated single-photon counting (TCSPC, FluoTime 200, PicoQuant GmbH). The fluorescence decay curves were fitted in Fluofit data analysis (Picoquant GmbH) software by a two-exponential model with reconvolution of the instrumental response function.

**2.3. Synthesis of Fl-APTES (Scheme 1A).** Commercial FAM-SE was converted to Fl-APTES by reaction with APTES. Briefly, in a 1.5 mL Eppendorf tube, 9.2 mg (19.4 $\mu$mol) of FAM-SE was dissolved in 196 $\mu$L of DMF. Then, 13.2 $\mu$L (94.7 $\mu$mol) of Et$_3$N and 3.2 $\mu$L (13.7 $\mu$mol) of APTES were sequentially added to the FAM-SE solution. The reaction was mechanically stirred at 1000 rpm for 24 h and subsequently diluted to 15 mL of EtOH without further purification. HRMS (ESI): $m/z$ calcd for $C_{30}H_{33}NO_9Si$ + H$^+$: 580.1997 [M + H]$^+$; found, 580.2038.

**2.4. Synthesis of SiO$_2$ NPs.** Silica nanoparticles (SiO$_2$ NPs) were synthesized according to the previously published Stöber condensation method.[66] Briefly, an 80 mM TEOS solution was prepared by adding 450 $\mu$L of TEOS to 25 mL of anhydrous EtOH in a 50 mL polypropylene conical tube. Then, 1.125 mL of nanopure water and 480 $\mu$L of NH$_4$OH were sequentially added to the TEOS solution and mechanically stirred at 300 rpm for 18 h. The reaction mixture was then purified through centrifugation (15 min, 12,000 RCF), washed thrice with ethanol, and redispersed in 25 mL of EtOH. The final SiO$_2$ NP concentration assessed by NTA was $(7.7 \pm 0.2) \times 10^{12}$ NP/mL.

**2.5. Synthesis of SiO$_2$@Fl NPs (Scheme 1B, Step I).** Fl-APTES was grafted to SiO$_2$@NPs using a simple condensation procedure. More precisely, 6.5 mL of freshly synthesized SiO$_2$ NPs was diluted to 38 mL with ethanol. To this dispersion were then injected sequentially 14 mL of a 0.91 mM Fl-APTES solution and 0.26 mL of NH$_4$OH. The mixture was mechanically stirred at 300 rpm for 24 h, purified through centrifugation (15 min, 12,000 RCF), and washed with ethanol

until no residual fluorescence was observed in the supernatant. The sample was redispersed in 10 mL of ethanol, corresponding to a final concentration of $(2.1 \pm 0.1) \times 10^{12}$ NP/mL.

**2.6. Synthesis of SiO$_2$@Fl-DTC and SiO$_2$@Fl (Control) NPs (Scheme 1B, Step II).** A 6 mL aliquot of the freshly synthesized SiO$_2$@Fl NPs was centrifugated and dried under vacuum at room temperature until complete evaporation of the solvent. The dried sample was then redispersed in 62 mL of anhydrous MeCN with vigorous agitation and sonication sequences. Then, 27 $\mu$L of a 57 mM DIPEA solution and 43 $\mu$L of a 72 mM PCTF solution were added to the SiO$_2$@Fl NP dispersion. For the SiO$_2$@Fl NP control sample, only the DIPEA solution was added, whereas the PCTF solution was omitted. The sealed reaction vessel was agitated mechanically at 300 rpm for 18 h. *In situ* fluorescence monitoring of the conversion from SiO$_2$@Fl to SiO$_2$@Fl-DTC was performed by periodically sampling 400 $\mu$L of either the reaction or control dispersion and diluting it in a 10 mm path quartz cuvette containing 2 mL of MeCN. Upon completion, the samples were purified by centrifugation (15 min, 12,000 RCF), washed thrice with MeCN, and redispersed in 10 mL of the latter. The concentrations of the final dispersions were $(2.26 \pm 0.04) \times 10^{11}$ NP/mL for SiO$_2$@Fl-DTC NPs and $(1.54 \pm 0.07) \times 10^{11}$ NP/mL for control SiO$_2$@Fl NPs.

**2.7. Synthesis of Ag NPs.** Ag NPs (70 nm) were prepared from an existing protocol by growing Ag seeds, with isolation of 20 nm and 50 nm particles in between.[26] For the seed formation, 75 mL of nanopure water and 20 mL of a 34 mM aqueous sodium citrate solution were placed in a 250 mL round-bottom flask and were heated to 70 °C under vigorous magnetic stirring (900 rpm). Upon stabilization of the temperature (∼10 min), 1.7 mL of 59 mM aqueous AgNO$_3$ and 0.2 mL of fresh 264 mM aqueous NaBH$_4$ were quickly added to the reaction flask. The mixture was stirred for 30 min, cooled to ambient temperature, and diluted to 100 mL with nanopure water. The Ag seeds, with a plasmon band centered at 389 nm and a diameter of 5−10 nm, were stored overnight in the dark at 4 °C to ensure deactivation of residual borohydride. To grow the particles to a diameter of ∼20 nm, 75 mL of nanopure water and 15 mL of the Ag seed solution were placed in a 250 mL round-bottom flask. The mixture was brought to a boil under reflux and vigorous stirring (900 rpm). Then, 2.0 mL of 34 mM aqueous sodium citrate was rapidly added to the mixture, followed 30 s later by the fast addition of 1.7 mL of 59 mM aqueous AgNO$_3$. The reaction was stirred under reflux for 60 min before being cooled back to ambient temperature and diluted to 100 mL with nanopure water. At this point, the silver nanoparticles' plasmon band remained centered at ∼390 nm. These particles were grown further to 50 nm by placing 74 mL of nanopure water and 25 mL of the freshly prepared 20 nm Ag particles in a 250 mL round-bottom flask heated at 90 °C under vigorous stirring (900 rpm). Then, 0.5 mL of 34 mM aqueous sodium citrate and 0.425 mL of 59 mM aqueous AgNO$_3$ were added sequentially to the vessel at a 15 s interval and stirred for 30 min. The mixture was then diluted by withdrawing 20 mL of the mixture from the vessel and adding 19 mL of nanopure water. After a 2 min stabilization period, additional aliquots of sodium citrate and AgNO$_3$ were added, as described above. These growth and dilution steps were repeated a total of 6 times, at which point the reaction was cooled to ambient temperature and diluted to 100 mL with nanopure water. At this point, the nanoparticles

**Scheme 1. Synthetic Route to Hg²⁺-Sensitive Fl-DTC Colloidal NPs, including the Synthetic Steps Performed in Solution (A) and as Colloidal Dispersions of Silica Nanoparticles (B) and Silver–Silica Core−Shell Nanoparticles (C)**
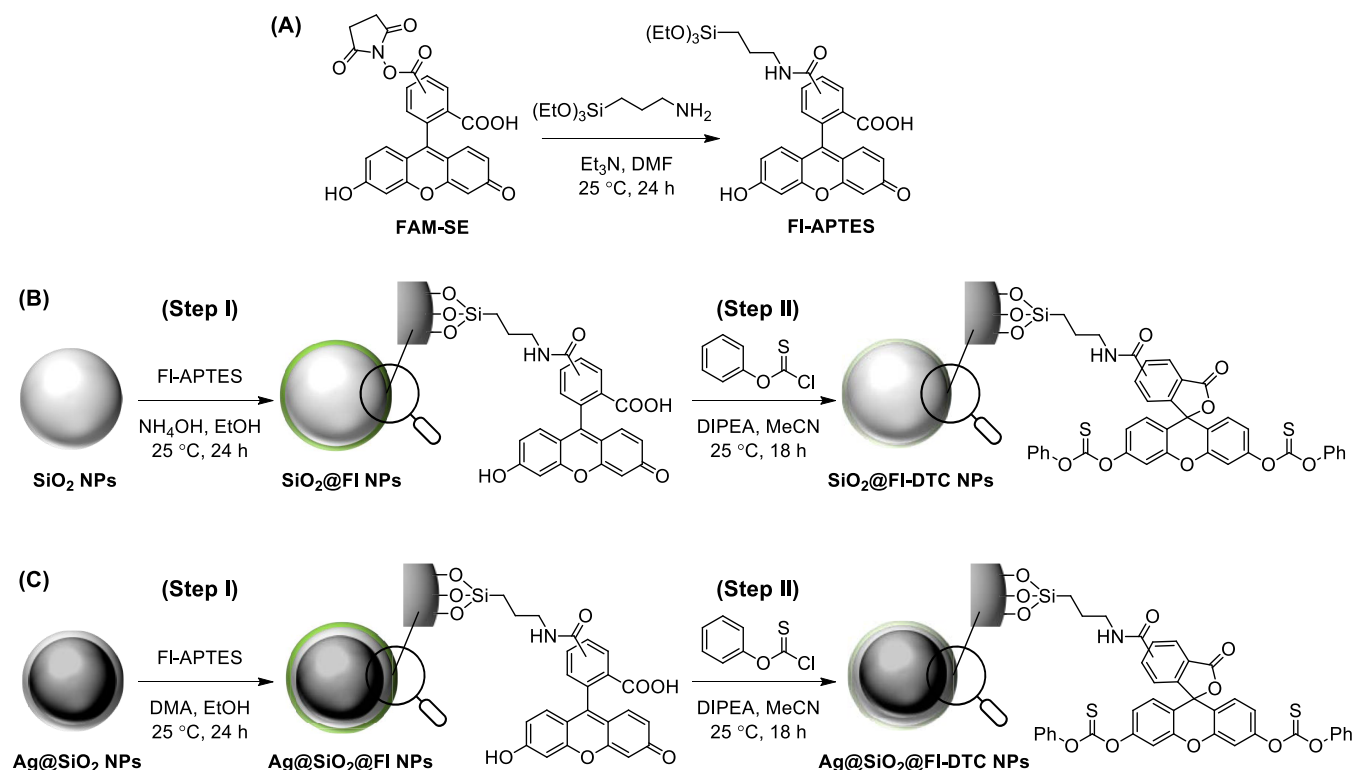


have a plasmon band centered at ∼432 nm. To generate the final 70 nm Ag NPs, the last growth step was performed by placing 47 mL of isolated 50 nm Ag NPs and 53 mL of nanopure water in a round-bottom flask heated at 85 °C with vigorous stirring (900 rpm). Then, 2.0 mL of 34 mM aqueous sodium citrate and 1.7 mL of 59 mM aqueous AgNO₃ were added, and the reaction was stirred for 2 h before being cooled down to ambient temperature. This final dispersion of 70 nm Ag NPs has a plasmon band centered at 454 nm and a concentration of $(1.14 \pm 0.03) \times 10^{11}$ NP/mL.

**2.8. Synthesis of Ag@SiO₂ NPs.** An 8 nm thick silica coating was deposited on Ag NPs using a previously published Stöber condensation method.[26] Briefly, a 0.13 mM TEOS solution was prepared by adding 10.2 mL of a 9 mM TEOS solution to 680 mL of anhydrous EtOH in a 1 L polypropylene bottle. Then, 85 mL of Ag NPs and 8.5 mL of aqueous DMA were sequentially added to the TEOS solution and mechanically stirred at 300 rpm for 18 h. The reaction mixture was then purified through centrifugation (10 min, 7000 RCF), washed twice with ethanol, and redispersed in 120 mL of EtOH. The final Ag@SiO₂ NP concentration assessed by NTA was $(4.1 \pm 0.1) \times 10^{10}$ NP/mL.

**2.9. Synthesis of Ag@SiO₂@Fl NPs (Scheme 1C, Step I).** Fl-APTES was grafted to Ag@SiO₂ NPs via a one-pot condensation procedure. More precisely, 97 mL of freshly synthesized Ag@SiO₂ NPs was diluted to 200 mL with ethanol. To this dispersion were then injected sequentially 3 mL of a 0.46 mM Fl-APTES solution and 1.4 mL of aqueous DMA. The mixture was mechanically stirred at 300 rpm for 24 h, purified through centrifugation (10 min, 7000 RCF), and washed with ethanol until no residual fluorescence was observed in the supernatant. The sample was redispersed in

45 mL of ethanol, corresponding to a final concentration of $(8.7 \pm 0.6) \times 10^{10}$ NP/mL.

**2.10. Synthesis of Ag@SiO₂@Fl-DTC and Ag@SiO₂@Fl (control) NPs (Scheme 1C, Step II).** The freshly synthesized Ag@SiO₂@Fl NPs (20 mL) were centrifugated and dried under vacuum at room temperature until complete evaporation of the solvent. The dried sample was then redispersed in 50 mL of anhydrous MeCN with vigorous agitation and sonication sequences. Then, 12 μL of a 57 mM DIPEA solution and 18 μL of a 72 mM PCTF solution were added to the Ag@SiO₂@Fl NP dispersion. For the Ag@SiO₂@Fl control NP sample, only the DIPEA solution was added, whereas the PCTF solution was omitted. The sealed reaction vessel was agitated mechanically at 300 rpm for 18 h. *In situ* fluorescence monitoring of the conversion from Ag@SiO₂@Fl to Ag@SiO₂@Fl-DTC was performed by periodically sampling 50 μL of either the reaction or control dispersion and diluting it in a 10 mm path quartz cuvette containing 2 mL of MeCN. Upon completion, the samples were purified by centrifugation (10 min, 7000 RCF), washed thrice with MeCN, and redispersed in 35 mL of the latter. The concentrations of the final dispersions were $(2.0 \pm 0.1) \times 10^{10}$ NP/mL for Ag@SiO₂@Fl-DTC NPs and $(1.7 \pm 0.1) \times 10^{10}$ NP/mL for control Ag@SiO₂@Fl NPs.

**2.11. Estimation of Fl Grafting Density on Colloidal Substrates.** The amount of dye molecules grafted onto each colloidal substrate was estimated by dissolving the silica matrix and performing standard fluorimetry on the liberated fluorophores. Briefly, a 400 μL aliquot of NPs (either SiO₂@Fl or Ag@SiO₂@Fl) of known concentration was added to 400 μL of aqueous 0.2 M NaOH. The mixture was stirred at 1000 rpm for 18 h at room temperature, and, when applicable, Ag cores were removed from the solution by centrifugation. Then,
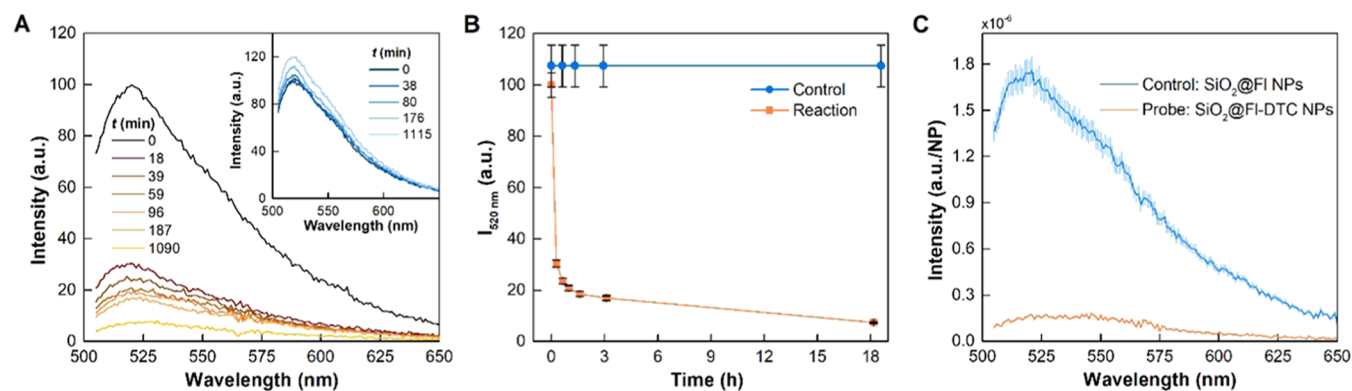
**Figure 1.** Fluorescence data of monitored and isolated products of the conversion of SiO$_2$@Fl NPs to SiO$_2$@Fl-DTC NPs. (A) Fluorescence spectra acquired during the reaction progress (inset: control dispersion of SiO$_2$@Fl NPs without PCTF), (B) fluorescence intensity at $\lambda_{em}$ = 520 nm as a function of time for both reaction and control, and (C) fluorescence spectra of the isolated probe and control after 18 h, with data normalized by their respective final particle concentration as measured by NTA. Error bars represent error propagation from the NTA measurements.

three 200 $\mu$L samples were each diluted with 2 mL of 0.1 M aqueous NaOH for fluorimetric analysis in triplicates. The calibration curve was performed with solutions of Fl-APTES in identical conditions (i.e., aqueous 0.1 M NaOH and stirred 18 h before use). The dye concentrations obtained for each sample were then adjusted according to their NP concentration and surface area to enable comparisons.

**2.12. Preparation of HEPES and Hg$^{2+}$ Stock Solutions.** The aqueous 20 mM HEPES buffer solution was prepared from the commercial salt. The pH was adjusted to 7.0 with an aqueous NaOH solution and a pH meter. Stock solutions of 2, 4, 6, 8, 10, 20, 30, 40, 50, 75, and 100 $\mu$M Hg$^{2+}$ were prepared from mercury(II) nitrate monohydrate dissolved in nanopure water.

**2.13. General Considerations for Kinetic Fluorescence Experiments.** Sample preparation for kinetic fluorescence monitoring proceeded as follows: 20 $\mu$L of a Hg$^{2+}$ stock solution (or a spiked real water sample) was added to 2 mL of HEPES buffer in a quartz cell placed in the spectrometer's sample compartment. The cuvette was then spiked with 40 $\mu$L of the colloidal sensor (either SiO$_2$@Fl-DTC NPs or Ag@SiO$_2$@Fl-DTC NPs), and a kinetic-based fluorescence acquisition was immediately performed for a total time of 60 s with a 2 s increment. The data was plotted as intensity ($I$) vs time ($t$), and the derivate was taken to report the kinetic rate $r$. All kinetic experiments were performed in replicates and averaged with the standard deviation as the uncertainty.

## 3. RESULTS AND DISCUSSION

**3.1. Synthesis of the Silica-Based Colloidal Hg$^{2+}$ Sensor (SiO$_2$@Fl-DTC NPs).** Silica nanoparticles (SiO$_2$ NPs) with a diameter of (70 ± 6) nm were synthesized by a Stöber condensation procedure to generate the model colloidal substrate. To append the coveted Hg$^{2+}$-sensitive Fl-DTC compound to SiO$_2$ NPs, the former must present a functionality allowing it to be covalently attached to the silica network. Fortunately, fluorescein is one of the most common dyes commercially available with a plethora of functional groups to enable its utilization for various applications. Although fluorescein isothiocyanate (FiTC) is the most common derivative, it was rejected in this study to avoid a potential competitive interaction of thiophilic mercury ions

with the dye's sulfurated site. Instead, fluorescein succinimidyl ester (FAM-SE), which reacts efficiently with primary amines, was chosen. Thus, FAM-SE was condensed with 3-aminopropyltriethoxysilane (APTES) and subsequently grafted onto SiO$_2$ NPs prior to the colloids being converted to their Hg$^{2+}$-sensitive state (Scheme 1). Although APTES is often condensed directly on silica substrates and subsequently reacted with a target moiety, the latter route was unfavorable in the present system, as thionocarbonate groups are prone to nucleophilic attack by primary amines. For instance, mass spectrometry revealed that dithionocarbonated fluorescein succinimidyl ester (DTC-FAM-SE) could be synthesized and isolated but decomposed upon contact with APTES (Supporting Information, SI, Figure S1). Thus, it was found preferable to convert the dye to a silane, Fl-APTES, and graft it to SiO$_2$ NPs before incorporating the thionocarbonate source in the system (Scheme 1).

The extent of dye incorporation on the fluorescent SiO$_2$ NPs (SiO$_2$@Fl NPs) was estimated by dissolving the silica matrix in aqueous sodium hydroxide and quantifying the liberated fluorophores by standard fluorimetry. From this experiment, a surface coverage of (30 ± 3) × 10$^1$ molecules/NP was determined. Conversion of SiO$_2$@Fl NPs to their Hg$^{2+}$-sensitive analog (SiO$_2$@Fl-DTC NPs) was then performed in a colloidal state using conditions typical for thionocarbonate formation from alcohol-containing compounds, i.e., with diisopropylethylamine (DIPEA) and o-phenyl chlorothionoformate (PCTF).[43,67,68] Although fluorescein is often illustrated in its quinoidal form, it exists as a tautomeric equilibrium with a spirolactone conformation displaying two hydroxyl groups. Therefore, reaction with sufficient PCTF molecules can produce two thionocarbonate moieties.[43] Compared to the bare fluorescein molecule, its dithionocarbonated counterpart is nonluminescent in the visible region due to a forced spirolactone backbone preventing tautomerization and electron delocalization (Scheme S2). Hence, this drastic alteration in optical properties from reactants to products allows to monitor the reaction progress by fluorimetry. Figure 1A shows fluorescence spectra acquired throughout the reaction from $t$ = 0 to 18 h. A control was performed by dispersing SiO$_2$@Fl NPs in the same reaction conditions but omitting PCTF. Results show that the control's fluorescence did not fluctuate significantly throughout the total reaction

time (∼8% deviation), whereas the signal of the reacting suspension decreased rapidly to 25% of its original intensity in less than an hour and reached ∼5% after 18 h (Figure 1B). At this point, the reaction was quenched by successive centrifugation and washing steps and redispersed to measure the fluorescence of the purified sample (Figure 1C).

From these data, the conversion efficiency of SiO$_2$@Fl NPs to SiO$_2$@Fl-DTC NPs was assessed from their relative fluorescence

$$\%conversion = \left(1 - \frac{I_{SiO_2@Fl-DTC}}{I_{SiO_2@Fl}}\right) \times 100\% \qquad (1)$$

where $I_{SiO_2@Fl\text{-}DTC}$ and $I_{SiO_2@Fl}$ are the fluorescence intensity at $\lambda_{em}$ = 520 nm of the purified probe and control samples, respectively. The calculated conversion of $(90 \pm 6)\%$ suggests a residual fluorescence from unconverted dye molecules at the surface of the isolated SiO$_2$@Fl-DTC NPs.

The physical parameters of the NPs described above are presented in Table 1. The particles' dry size ($d$) and

**Table 1. Physical Parameters of Studied Silica Colloids$^a$**

| samples | $d$ (nm) | $D_H$ (nm) | $\zeta$ (mV) |
|---|---|---|---|
| SiO$_2$ NPs | 70 ± 6 | (9 ± 2) × 10$^1$ | −45 ± 8 |
| SiO$_2$@Fl NPs | 72 ± 6 | (9 ± 2) × 10$^1$ | −31 ± 6 |
| SiO$_2$@Fl-DTC NPs | 71 ± 6 | (13 ± 3) × 10$^1$ | −26 ± 6 |

$^a$Uncertainties correspond to the standard deviation of the mean. All histograms are available in the SI.

hydrodynamic size ($D_H$) were assessed by TEM and NTA, respectively. No significant modification of size was observed within the measurement error after functionalization. However, the $D_H$ of SiO$_2$@Fl-DTC NPs showed a slight shift to higher sizes with a broader standard deviation compared to its precursors. This is most likely due to the preliminary drying process required to provide the anhydrous conditions needed by the reaction of SiO$_2$@Fl NPs with PCTF. Indeed, SiO$_2$@Fl control NPs, when redispersed after drying, produced a similarly broadened size histogram (Figure S3D in SI), suggesting mild aggregation of the samples. The $\zeta$-potential of the series of samples was measured at pH 7.0, with pristine SiO$_2$ NPs showing a value of $(-45 \pm 8)$ mV, typical of silica particles synthesized by the Stöber method.[69] Condensation of Fl and further transformation to Fl-DTC induced a slight increase in $\zeta$ for each step, yet still in the range of values considered stable for an efficient repulsion between colloids (i.e., $\leq -30$ mV).

**3.2. Hg$^{2+}$-Sensing from a SiO$_2$@Fl-DTC NP Colloidal Dispersion.** The response of coreless SiO$_2$@Fl-DTC NPs to Hg$^{2+}$ was first assessed by placing a $(4.39 \pm 0.07) \times 10^9$ NP/mL dispersion of the probe in contact with 1 $\mu$M Hg$^{2+}$ in a HEPES buffer solution (20 mM, pH 7.0, 2% MeCN). Figure 2A shows the temporal evolution of the system's fluorescence as the contact time between the probe and the analyte increased. The presence of Hg$^{2+}$ caused an increase in fluorescence, rising continuously for over 90 min. This behavior is also observed for freely diffusing Fl-DTC in contact with Hg$^{2+}$ in similar conditions.[43] For sensing purposes, this long reaction time can be mitigated by measuring the fluorescence response kinetically. By recording the first derivative of the time-dependent fluorescence instead of the absolute fluorescence at a given time, the analysis time
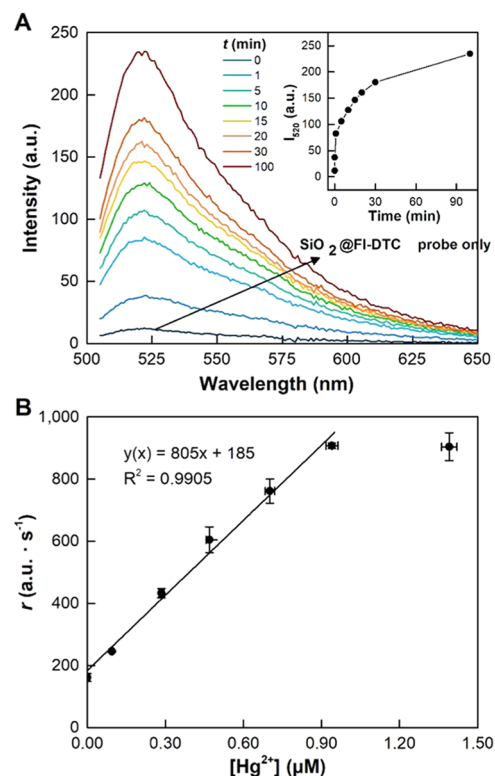


**Figure 2.** (A) Time-dependent fluorescence spectra of a dispersion of SiO$_2$@Fl-DTC NPs with 1 $\mu$M Hg$^{2+}$. Inset: time-dependent fluorescence at $\lambda_{em}$ = 520 nm. (B) Reaction kinetics $r$ of SiO$_2$@Fl-DTC NPs as a function of the concentration of Hg$^{2+}$ in the range 0–1.50 $\mu$M. Error bars represent RSD ($n = 3$). Conditions: $(4.39 \pm 0.07) \times 10^9$ NP/mL dispersion in 20 mM HEPES buffer, pH 7.0, 2% MeCN.

can be reduced to <1 min. To this end, the kinetic rate, denoted $r$, was extrapolated from the first minute of contact with Hg$^{2+}$ and acted as the measured variable for further fluorescence experiments.

The sensitivity of coreless SiO$_2$@Fl-DTC NPs toward Hg$^{2+}$ quantification was assessed by a calibration curve ranging from 0 to 1.5 $\mu$M Hg$^{2+}$ in a 20 mM HEPES buffer (pH 7.0, 2% MeCN) (Figure 2B). Results show a linear curve up to 1 $\mu$M, at which point the kinetic rate $r$ reaches a plateau. On the lower end of the dynamic range, a detection limit of 50 nM was calculated ($3\sigma_{blank}$/slope). The limiting factor to this value is the autohydrolysis of the thionocarbonate moieties in the absence of the analyte. Indeed, a blank measurement of SiO$_2$@Fl-DTC NPs in the HEPES buffer afforded a non-null $r$ value, suggesting spontaneous hydrolysis. This behavior is inherent to the Fl-DTC moiety, as its intrinsic Hg$^{2+}$ sensing mechanism relies on thionocarbonate hydrolysis accelerated by the binding of the target ion to its sulfurated site.[43] For the purpose of this work, these results show unequivocally that quantification of Hg$^{2+}$ can be achieved by immobilizing a Hg$^{2+}$-sensitive fluorescein onto a colloidal substrate. The analytical performance of this coreless nanoprobe, as it stands, remains insufficient for quantitative analysis of Hg$^{2+}$ in drinking water at or below the threshold recommended by the WHO, which is one order of magnitude below the LOD reached with this nonplasmonic nanoprobe.

**3.3. Preparation and Fluorescence Enhancement Properties of Ag@SiO$_2$@Fl NPs.** To provide an optimal

core−shell morphology for MEF, silver nanoparticles (Ag NPs) with a diameter of $(7 \pm 1) \times 10^1$ nm were synthesized by a seeded growth method and subsequently coated with an $(8 \pm 1)$-nm-thick layer of silica through Stöber condensation to generate core−shell Ag@SiO$_2$ NPs (Figure 3A). UV−visible
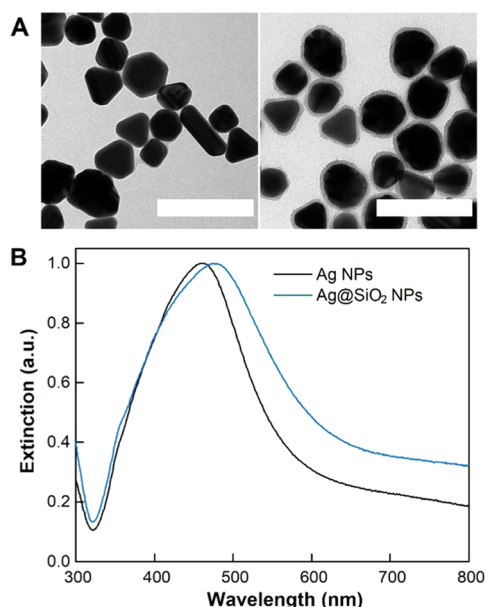


**Figure 3.** (A) TEM micrographs of Ag NP cores (left) and core−shell Ag@SiO$_2$ NPs (right) and (B) their corresponding normalized extinction spectra. Scale bars are 200 nm.

spectrometry was performed to assess changes in the surrounding conditions and the occurrence of aggregation of the colloids throughout their preparation. As shown in Figure 3B, the extinction spectrum of Ag cores displayed a band centered at 459 nm, corresponding to the LSPR of the dispersion. The band was red-shifted to 476 nm upon coating with SiO$_2$ due to the associated change in the refractive index.[15] Fl-APTES was then condensed onto the Ag@SiO$_2$ NPs using the same strategy as for the model SiO$_2$ NPs, generating fluorescent Ag@SiO$_2$@Fl NPs with a surface coverage of $(20 \pm 2) \times 10^2$ molecules/NP.

To characterize the extent of signal enhancement, steady-state and time-resolved fluorescence measurements were performed on the emissive SiO$_2$@Fl NPs and Ag@SiO$_2$@Fl NPs since their thionocarbonated counterparts were barely emissive. Using these probe precursors still gave a valid estimate of the fluorescence behavior upon Hg$^{2+}$ detection, considering that Fl emission is recovered after hydrolysis of the thionocarbonate groups. As displayed in Figure 4, individual silver-core particles were 14 times more fluorescent than the silica-based model. However, this observation cannot be solely attributed to MEF since a comparison of Fl dye surface coverage values attest that Ag-core colloids contained a higher dye amount per NP than the solid silica spheres (Table 2). This can be explained by the larger overall diameter of Ag@SiO$_2$@Fl NPs compared to SiO$_2$@Fl NPs, implying a larger surface available for grafting. Even so, when adjusting dye count for the NPs' approximated surface area, Ag@SiO$_2$@Fl NPs still exhibit a greater Fl grafting density than that of SiO$_2$@Fl NPs (Table 2). The discrepancy may arise from the different experimental conditions used to generate the silica matrix, possibly affecting porosity and reactivity toward Fl-
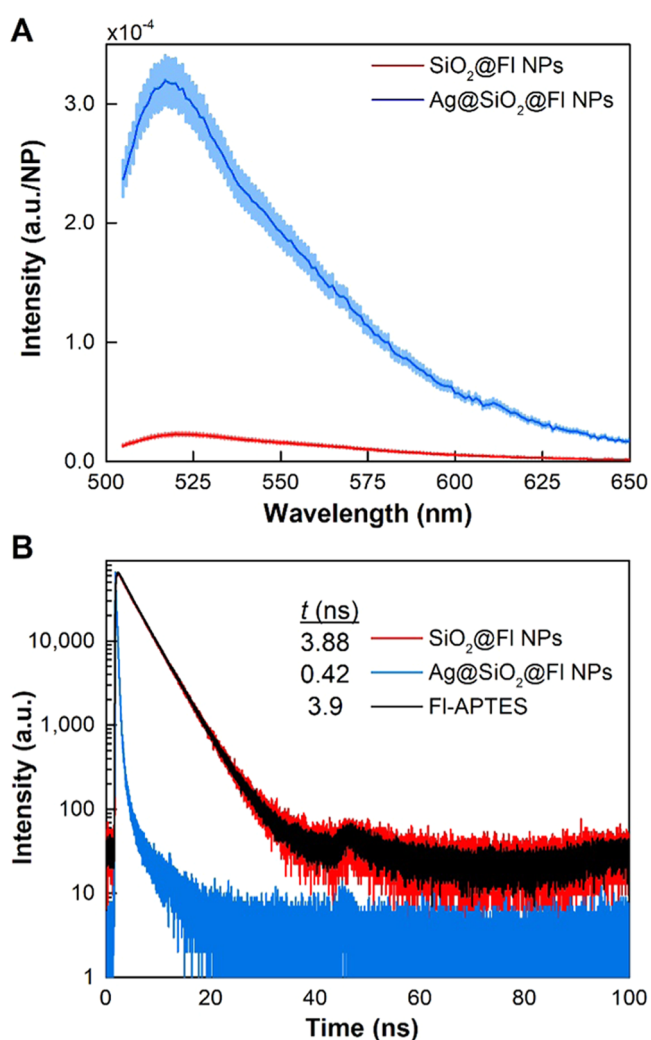


**Figure 4.** (A) Fluorescence spectra of SiO$_2$@Fl NPs and Ag@SiO$_2$@Fl NPs in 20 mM HEPES buffer and (B) their fluorescence decay curves compared to aqueous Fl-APTES. Spectra are normalized by their respective particle concentration measured through NTA and error bars represent error propagation from these measurements.

**Table 2. Surface Coverage of Fl on Colloidal Substrates**

| | Fl dye amount (molecules/NP) | Fl grafting density$^a$ (μmol/m$^2$) |
|---|---|---|
| SiO$_2$@Fl NPs | $(31 \pm 3) \times 10^1$ | $0.031 \pm 0.003$ |
| Ag@SiO$_2$@Fl NPs | $(20 \pm 2) \times 10^2$ | $0.13 \pm 0.01$ |

$^a$These values are calculated using the NPs' surface area extrapolated from TEM size distributions assuming spherical objects. However, the Ag-core sample has a more polydisperse morphology than SiO$_2$-only NPs, possibly limiting the accuracy of this approach.

APTES. As obtaining a sufficient mass of Ag@SiO$_2$ NPs for Brunauer−Emmett−Teller (BET) surface area analysis is laborious, the hypothesis that the latter's porosity is greater than that of the synthesized SiO$_2$ NPs to accommodate more Fl dye was not pursued further. Ultimately, the above-mentioned assessments demonstrate that the sole comparison of the steady-state fluorescence of the two systems is an inadequate approach to corroborate the manifestation of MEF in Ag@SiO$_2$@Fl NPs.

Along with overall fluorescence enhancement, MEF is also known for quickening excited-state radiative decay, as the

presence of the metal core allows additional emissive relaxation pathways limiting nonradiative contributions. Time-resolved fluorescence decay curves were acquired for SiO$_2$@Fl NPs, Ag@SiO$_2$@Fl NPs, and solution-state Fl-APTES (Figure 4B and Table S2 in SI). Results demonstrate a decrease in the fluorescence lifetime with the silver-core sample. Whereas fluorescein moieties grafted to solid silica spheres show a lifetime of 3.88 ± 0.02 ns, statistically identical to that of free molecular Fl-APTES (3.9 ± 0.2 ns), Ag@SiO$_2$@Fl probes display a fluorescence lifetime of 0.42 ± 0.2 ns, consistent with other Fl-appended silver-core systems reported in the literature.[26,28] Moreover, the magnitude of the decrease caused by MEF is greater than that previously reported for a Hg$^{2+}$-sensitive Ag-doped mesoporous silica network,[59] where the MEF probe produced a decrease in the lifetime of rhodamine dye from 1.95 to 1.65 ns. The above results suggest that integrating considerations of plasmonic core size and dye-core distance in the design of the Hg$^{2+}$-sensitive probes can lead to substantial improvements in photostability.

### 3.4. Preparation of a Colloidal Core–Shell Hg$^{2+}$ Sensor (Ag@SiO$_2$@Fl-DTC NPs).

Ag@SiO$_2$@Fl colloids were converted to their Hg$^{2+}$-sensitive form (Ag@SiO$_2$@Fl-DTC NPs) using the same strategy as for the model SiO$_2$ NPs, i.e., by reacting the particle dispersion with PCTF (Scheme 1C). Reaction progress monitored through fluorescence measurements showed a behavior like that of the SiO$_2$@Fl-DTC NP synthesis, i.e., a significant decrease in fluorescence intensity over 18 h compared to the control dispersion without PCTF (Figure 5A). After purification, we calculated a conversion of (90 ± 9)% from the fluorescence data for the probe and control samples, a value matching that of the solid silica sphere model. Hence, the inclusion of a silver core did not impact the conversion efficiency of the dye to its Hg$^{2+}$-sensitive form.

Physical parameters of silver-core NPs were assessed through TEM, NTA, UV–visible spectrometry, and $\zeta$ analysis (Table 3 and Figures S4–S6). Like the solid silica model, no significant modification to particle size was observed within measurement error, and the $\zeta$ values remained in a range (−35 to −30 mV) indicative of a stable suspension for negatively charged surfaces. The plasmon band recorded by UV–visible spectroscopy between each preparation step also indicated no significant changes further than that expected by the preliminary silica coating on the silver cores. A slight broadening of the plasmon band of Ag@SiO$_2$@Fl-DTC NPs was observed compared to its precursor (Figure S6), which is most likely due to slight aggregation caused by the required particle drying step to induce conversion of the dye to its Hg$^{2+}$ sensing form.

Following the preparation and characterization of the prepared Ag@SiO$_2$@Fl-DTC NPs, their reaction to Hg$^{2+}$ was evaluated qualitatively by placing a (3.9 ± 0.2) × 10$^8$ NP/mL colloidal dispersion in contact with 50 nM Hg$^{2+}$ in a HEPES buffer solution (20 mM, pH 7.0, 2% MeCN). Figure 6A shows that the system's fluorescence increased with contact time in a behavior like that observed for our silica-based model (Figure 2A). As discussed for Hg$^{2+}$ sensing with SiO$_2$@Fl-DTC NPs, conveying the initial fluorescence kinetic rate $r$ instead of the absolute fluorescence intensity allows to decrease the Hg$^{2+}$ response time to <1 min to facilitate quantification and applicability to tangible situations. In this regard, the potential of Ag@SiO$_2$@Fl-DTC NPs to quantify Hg$^{2+}$ was assessed through a calibration curve plotting $r$ against
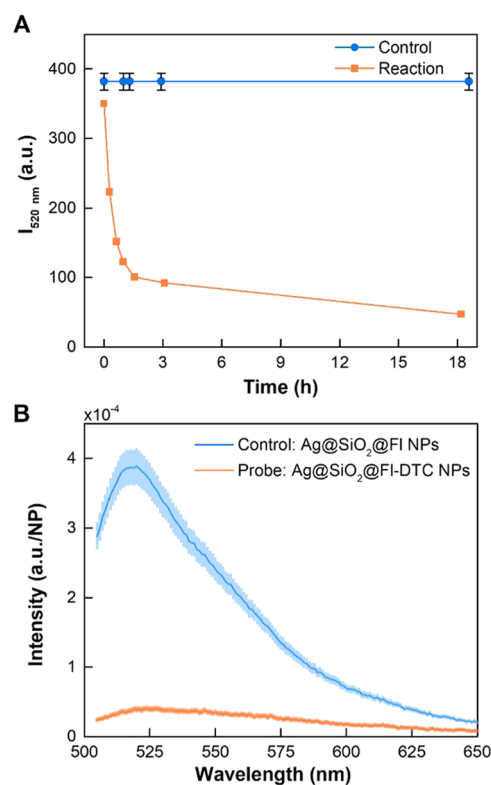


**Figure 5.** (A) Fluorescence intensity at $\lambda_{em}$ = 520 nm as a function of time for the conversion of Ag@SiO$_2$@Fl NPs to Ag@SiO$_2$@Fl-DTC NPs and for a control sample of Ag@SiO$_2$@Fl NPs without PCTF. (B) Fluorescence spectra of the isolated probe and control in MeCN, with data normalized by their respective final particle concentration as measured by NTA. Error bars represent error propagation from the NTA measurements.

Hg$^{2+}$ in concentrations ranging from 0 to 1 $\mu$M in a HEPES buffer (20 mM, pH 7.0, 2% MeCN). Results show a linear relationship up to ∼ 0.3 $\mu$M. This upper limit may seem subsided compared to the model SiO$_2$@Fl-DTC NPs, but this observation is related to a discrepancy in the total amount of the Fl-DTC probe in both systems. Essentially, when considering NP concentration and dye coverage, the total amount of Hg$^{2+}$-sensitive Fl-DTC available during calibration is lower for the silver-core system than for the silica-based model. As for many analytical probes, the dynamic range of detection is related to the former's concentration and can be tuned if required. In the results presented herein, the most striking difference is the sensitivity (i.e., the slope), which is >6 times higher for Ag@SiO$_2$@Fl-DTC NPs than for SiO$_2$@Fl-DTC NPs even though the former has a lower probe count in the presented data. This observation is caused by the occurrence of MEF in the Ag-core nanoparticles, implying greater emission with each detection event, thus leading to higher apparent $r$ values at all Hg$^{2+}$ concentrations. Overall, this highly emissive system operates at a lower NP concentration than the silica model, which compensates amply for the added complexity and higher cost of the Ag@SiO$_2$ NP synthesis. Additionally, a LOD of 2 nM Hg$^{2+}$ was achieved with Ag@SiO$_2$@Fl-DTC NPs, a significant improvement over the 50 nM LOD obtained for SiO$_2$@Fl-DTC NPs and a satisfactory upgrade to meet WHO's drinking water regulations.

**Table 3. Physical Parameters of Studied Silver-Core Colloids**[a]

| samples | $d$ (nm)[b] | $l$ (nm)[c] | $D_H$ (nm) | $\zeta$ (mV) | $\lambda_{max}$ (nm) |
|---|---|---|---|---|---|
| Ag NPs | $(7 \pm 1) \times 10^1$ | | $(8 \pm 2) \times 10^1$ | $-35 \pm 9$ | 455 |
| Ag@SiO$_2$ NPs | $(7 \pm 1) \times 10^1$ | $8 \pm 1$ | $(11 \pm 4) \times 10^1$ | $-32 \pm 6$ | 476 |
| Ag@SiO$_2$@Fl NPs | $(7 \pm 1) \times 10^1$ | $8 \pm 1$ | $(11 \pm 4) \times 10^1$ | $-31 \pm 7$ | 476 |
| Ag@SiO$_2$@Fl-DTC NPs | $(7 \pm 1) \times 10^1$ | $8 \pm 1$ | $(12 \pm 4) \times 10^1$ | $-30 \pm 7$ | 476 |

[a]Uncertainties correspond to the standard deviation of the mean. All relevant histograms and spectra are available in the SI. [b]$d$: diameter of the Ag core. [c]$l$: thickness of the silica shell.
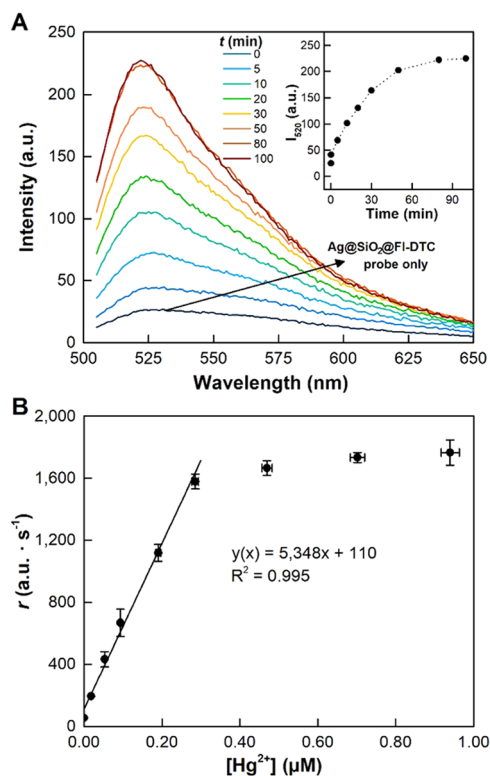


**Figure 6.** (A) Time-dependent fluorescence spectra of a dispersion of Ag@SiO$_2$@Fl-DTC NPs with 50 nM Hg$^{2+}$. Inset: time-dependent fluorescence at $\lambda_{em}$ = 520 nm. (B) Reaction kinetics $r$ of Ag@SiO$_2$@Fl-DTC NPs as a function of the concentration of Hg$^{2+}$ in the range 0−1.00 μM. Error bars represent RSD ($n$ = 3). Conditions: $(3.9 \pm 0.2) \times 10^8$ NP/mL dispersion in 20 mM HEPES buffer, pH 7.0, 2% MeCN.

**3.5. Operational Considerations and Application to Real Water Samples.** To assess Ag@SiO$_2$@Fl-DTC NPs for analyzing water samples in actual field conditions, probe response was examined at pH values between 3 and 10 (Figure S7). As expected, the fluorescence decreases from pH 7 to 3 due to fluorescein's intrinsic pH sensitivity in this range.[70] Conversely, increasing the pH from 7 to 10 negatively impacts the sensor's response to Hg$^{2+}$ due to an increase in spontaneous hydrolysis and the formation of mercury hydroxide.[71] This pH profile fits with that obtained for molecular Fl-DTC reported elsewhere[43] and indicates that it is preferable to perform measurements in the vicinity of neutral pH to maximize the performance of the probe.

The selectivity of Ag@SiO$_2$@Fl-DTC NPs to Hg$^{2+}$ cations and tolerance to interfering species were also assessed by testing the probe against 21 other cations (Figure S8). On the one hand, the results show that the MEF-enabled probe responds strongly to Hg$^{2+}$ ions but also slightly to Ag$^+$ ions at equivalent concentrations. The behavior stems from the

intrinsic thiophilic nature of the ions, and response from Au$^{3+}$ ions would therefore also be expected. On the other hand, the interference study showed that adding a 4-fold excess of Ag$^+$ during Hg$^{2+}$ sensing has a negligible effect. Combined with the scarce presence of noble metals in the environment, this selectivity feature is not deemed troublesome for real-world applications.[72] No ambiguity or variability loomed from the presence of metallic silver at the core of the probe either.

As a final demonstration, the probe was tested with real water samples from Saint-Charles Lake and the Saint-Charles River (Québec City, Québec, Canada) to evaluate its applicability to complex matrices while avoiding extended sample preparation. A table of the major ionic components of these samples is provided in the SI. As Hg$^{2+}$ was undetectable in the collected samples, experiments were performed by adding either 2 or 20 μM of Hg$^{2+}$ in the filtered lake and river water samples and spiking this fortified solution in the Hg$^{2+}$-sensitive plasmonic colloid solution (20 mM HEPES buffer, pH 7.0, 2% MeCN). Table 4 compiles the expected and measured Hg$^{2+}$ concentrations, where recovery values contiguous to 100% suggest that the approach is compatible with real water conditions.

**Table 4. Analysis Results of Hg$^{2+}$ in Natural Water Samples Using Ag@SiO$_2$@Fl-DTC NPs**[ab]

| water sample | Hg$^{2+}$ added (μM) | Hg$^{2+}$ found (μM) | recovery (%) |
|---|---|---|---|
| A[a] | none | <LOD | N/A |
| | $1.98 \pm 0.02$ | $2.62 \pm 0.07$ | $132 \pm 5$ |
| | $20.1 \pm 0.2$ | $20 \pm 1$ | $101 \pm 7$ |
| B[b] | none | <LOD | N/A |
| | $1.98 \pm 0.02$ | $2.0 \pm 0.1$ | $102 \pm 6$ |
| | $20.1 \pm 0.2$ | $19 \pm 01$ | $95 \pm 6$ |

[a]Filtered water from Saint-Charles Lake in Québec City, Québec, Canada. [b]Filtered water from Saint-Charles River in Québec City, Québec, Canada.

## 4. CONCLUSIONS

To summarize, a silver-core silica-shell nanoarchitecture was developed to expand the advantages offered by colloidal platforms and MEF for Hg$^{2+}$ sensing using a fluorescein derivative. Both a core−shell architecture and a SiO$_2$ solid sphere model substrate were synthesized, and the emissive dye was grafted to both colloidal structures and converted into the nonemissive Hg$^{2+}$-sensitive dithionocarbonated form with a conversion yield greater than 90%. The isolated nanoprobes were subjected to qualitative and quantitative Hg$^{2+}$ sensing, where LODs of 50 and 2 nM were calculated for the SiO$_2$ and Ag@SiO$_2$ systems, respectively. Testing with natural water samples also showed the suitability of the silver-core probe for analyzing complex matrices such as those encountered in real applications. Interestingly, steady-state and time-resolved

fluorescence measurements showed that fluorescence intensity was increased by a factor of 14 and the excited-state lifetime was decreased by 9 times, due to plasmon-induced acceleration of the radiative decay rate of the $Hg^{2+}$ fluorogenic sensor. This work was performed with a dye that is intrinsically quite emissive ($\Phi$ = 93%), but combining plasmonic core–shell nanoarchitectures with other $Hg^{2+}$-sensitive fluorescent probes could provide an additional advantage when the molecular dye involved has a low quantum yield. As a result of the plethora of dyes and plasmonic structures amenable to the design of MEF-enabled chemical nanoprobes, a variety of particle–dye combinations are conceivable.

## ASSOCIATED CONTENT

### Supporting Information

The Supporting Information is available free of charge at https://pubs.acs.org/doi/10.1021/acsomega.2c02985.

Isolation of DTC-FAM-SE and condensation attempt with APTES, physical properties of colloidal substrates (TEM micrographs, size distribution histograms, NP concentration histograms, and UV–visible spectra), pH dependency, selectivity and interference study, natural water sample data, TCSPC-related data, and additional schemes (PDF)

## AUTHOR INFORMATION

### Corresponding Author

**Denis Boudreau** − *Département de chimie and Centre d'optique, photonique et laser (COPL), Université Laval, Québec, QC G1V 0A6, Canada;* orcid.org/0000-0001-5152-2464; Email: denis.boudreau@chm.ulaval.ca

### Authors

**Audrey Picard-Lafond** − *Département de chimie and Centre d'optique, photonique et laser (COPL), Université Laval, Québec, QC G1V 0A6, Canada*

**Dominic Larivière** − *Département de chimie, Université Laval, Québec, QC G1V 0A6, Canada;* orcid.org/0000-0003-1860-1181

Complete contact information is available at:
https://pubs.acs.org/10.1021/acsomega.2c02985

### Author Contributions

Audrey Picard-Lafond: methodology, experiments, analysis, and writing. Dominic Larivière: supervision, reviewing. Denis Boudreau: supervision, funding, and reviewing.

### Notes

The authors declare no competing financial interest.

## ACKNOWLEDGMENTS

## REFERENCES

(1) Wu, D.; Sedgwick, A. C.; Gunnlaugsson, T.; Akkaya, E. U.; Yoon, J.; James, T. D. Fluorescent Chemosensors: The Past, Present and Future. *Chem. Soc. Rev.* **2017**, *46*, 7105−7123.

(2) Fu, Y.; Finney, N. S. Small-Molecule Fluorescent Probes and Their Design. *RSC Adv.* **2018**, *8*, 29051−29061.

(3) Lakowicz, J. R. Quenching of Fluorescence. In *Principles of Fluorescence Spectroscopy*, 3rd ed.; Lakowicz, J. R., Ed.; Springer: Boston, 2006; pp 277−330.

(4) Sharma, P.; Brown, S.; Walter, G.; Santra, S.; Moudgil, B. Nanoparticles for Bioimaging. *Adv. Colloid Interface Sci.* **2006**, *123−126*, 471−485.

(5) Avnir, D.; Kaufman, V. R.; Reisfeld, R. Organic Fluorescent Dyes Trapped in Silica and Silica-Titania Thin Films by the Sol-Gel Method. Photophysical, Film and Cage Properties. *J. Non-Cryst. Solids* **1985**, *74*, 395−406.

(6) Santra, S.; Dutta, D.; Moudgil, B. M. Functional Dye-Doped Silica Nanoparticles for Bioimaging, Diagnostics and Therapeutics. *Food Bioprod. Process.* **2005**, *83*, 136−140.

(7) Zhao, X.; Bagwe, R. P.; Tan, W. Development of Organic-Dye-Doped Silica Nanoparticles in a Reverse Microemulsion. *Adv. Mater.* **2004**, *16*, 173−176.

(8) Montalti, M.; Rampazzo, E.; Zaccheroni, N.; Prodi, L. Luminescent Chemosensors Based on Silica Nanoparticles for the Detection of Ionic Species. *New J. Chem.* **2013**, *37*, 28−34.

(9) Montalti, M.; Prodi, L.; Rampazzo, E.; Zaccheroni, N. Dye-Doped Silica Nanoparticles as Luminescent Organized Systems for Nanomedicine. *Chem. Soc. Rev.* **2014**, *43*, 4243−4268.

(10) Li, L.; Wang, W.; Tang, J.; Wang, Y.; Liu, J.; Huang, L.; Wang, Y.; Guo, F.; Wang, J.; Shen, W.; Belfiore, L. A. Classification, Synthesis, and Application of Luminescent Silica Nanoparticles: A Review. *Nanoscale Res. Lett.* **2019**, *14*, No. 190.

(11) Melhuish, W. H. Quantum Efficiencies of Fluorescence of Organic Substances: Effect of Solvent and Concentration of the Fluorescent Solute. *J. Phys. Chem. A* **1961**, *65*, 229−235.

(12) Imhof, A.; Megens, M.; Engelberts, J. J.; de Lang, D. T. N.; Sprik, R.; Vos, W. L. Spectroscopy of Fluorescein (FITC) Dyed Colloidal Silica Spheres. *J. Phys. Chem. B* **1999**, *103*, 1408−1415.

(13) Viger, M. L.; Live, L. S.; Therrien, O. D.; Boudreau, D. Reduction of Self-Quenching in Fluorescent Silica-Coated Silver Nanoparticles. *Plasmonics* **2008**, *3*, 33−40.

(14) Martini, M.; Perriat, P.; Montagna, M.; Pansu, R.; Julien, C.; Tillement, O.; Roux, S. How Gold Particles Suppress Concentration Quenching of Fluorophores Encapsulated in Silica Beads. *J. Phys. Chem. C* **2009**, *113*, 17669−17677.

(15) Kelly, K. L.; Coronado, E.; Zhao, L. L.; Schatz, G. C. The Optical Properties of Metal Nanoparticles: The Influence of Size, Shape, and Dielectric Environment. *J. Phys. Chem. B* **2003**, *107*, 668−677.

(16) Lakowicz, J. R.; Ray, K.; Chowdhury, M.; Szmacinski, H.; Fu, Y.; Zhang, J.; Nowaczyk, K. Plasmon-Controlled Fluorescence: A New Paradigm in Fluorescence Spectroscopy. *Analyst* **2008**, *133*, 1308−1346.

(17) Aslan, K.; Gryczynski, I.; Malicka, J.; Matveeva, E.; Lakowicz, J. R.; Geddes, C. D. Metal-Enhanced Fluorescence: An Emerging Tool in Biotechnology. *Curr. Opin. Biotechnol.* **2005**, *16*, 55−62.

(18) Jeong, Y.; Kook, Y. M.; Lee, K.; Koh, W. G. Metal Enhanced Fluorescence (MEF) for Biosensors: General Approaches and a Review of Recent Developments. *Biosens. Bioelectron.* **2018**, *111*, 102−116.

(19) Knoblauch, R.; Geddes, C. D. Review of Advances in Metal-Enhanced Fluorescence. In *Reviews in Plasmonics 2017*, Geddes, C. D., Ed.; Springer: Cham, 2019; pp 253−283.

(20) Contreras-Caceres, R.; Alonso-Cristobal, P.; Mendez-Gonzalez, D.; Laurenti, M.; Maldonado-Valdivia, A.; Garcia-Blanco, F.; López Cabarcos, E.; Fernandez-Barbero, A.; Lopez-Romero, J. M.; Rubio-Retama, J. Temperature Controlled Fluorescence on Au@Ag@PNIPAM-PTEBS Microgels: Effect of the Metal Core Size on the MEF Extension. *Langmuir* **2014**, *30*, 15560−15567.

(21) Sultangaziyev, A.; Bukasov, R. Review: Applications of Surface-Enhanced Fluorescence (SEF) Spectroscopy in Bio-Detection and Biosensing. *Sens. Bio-Sens. Res.* **2020**, *30*, No. 100382.

(22) Badshah, M. A.; Koh, N. Y.; Zia, A. W.; Abbas, N.; Zahra, Z.; Saleem, M. W. Recent Developments in Plasmonic Nanostructures for Metal Enhanced Fluorescence-Based Biosensing. *Nanomaterials* **2020**, *10*, No. 1749.

(23) Goulet, P. J. G.; Aroca, R. F. Surface-Enhancement of Fluorescence Near Noble Metal Nanostructures. In *Radiative Decay Engineering*, Geddes, C. D.; Lakowicz, J. R., Eds.; Springer: Boston, 2005; pp 223−247.

(24) Lessard-Viger, M.; Rioux, M.; Rainville, L.; Boudreau, D. FRET Enhancement in Multilayer Core−Shell Nanoparticles. *Nano Lett.* **2009**, *9*, 3066−3071.

(25) L-Vige, M.; Brouard, D.; Boudreau, D. Plasmon-Enhanced Resonance Energy Transfer from a Conjugated Polymer to Fluorescent Multilayer Core−Shell Nanoparticles: A Photophysical Study. *J. Phys. Chem. C* **2011**, *115*, 2974−2981.

(26) Asselin, J.; Legros, P.; Grégoire, A.; Boudreau, D. Correlating Metal-Enhanced Fluorescence and Structural Properties in Ag@SiO2 Core-Shell Nanoparticles. *Plasmonics* **2016**, *11*, 1369−1376.

(27) Pribik, R.; Dragan, A. I.; Zhang, Y.; Gaydos, C.; Geddes, C. D. Metal-Enhanced Fluorescence (MEF): Physical Characterization of Silver-Island Films and Exploring Sample Geometries. *Chem. Phys. Lett.* **2009**, *478*, 70−74.

(28) Dragan, A. I.; Bishop, E. S.; Casas-Finet, J. R.; Strouse, R. J.; McGivney, J.; Schenerman, M. A.; Geddes, C. D. Distance Dependence of Metal-Enhanced Fluorescence. *Plasmonics* **2012**, *7*, 739−744.

(29) Yan, Y.; Meng, L.; Zhang, W.; Zheng, Y.; Wang, S.; Ren, B.; Yang, Z.; Yan, X. High-Throughput Single-Particle Analysis of Metal-Enhanced Fluorescence in Free Solution Using Ag@SiO2 Core−Shell Nanoparticles. *ACS Sens.* **2017**, *2*, 1369−1376.

(30) Cheng, D.; Xu, Q.-H. Separation Distance Dependent Fluorescence Enhancement of Fluorescein Isothiocyanate by Silver Nanoparticles. *Chem. Commun.* **2007**, 248−250.

(31) Tu, S.; Rioux, D.; Perreault, J.; Brouard, D.; Meunier, M. Fluorescence and Scattering Dual-Mode Multiplexed Imaging with Gold-Silver Alloy Core Silica Shell Nanoparticles. *J. Phys. Chem. C* **2017**, *121*, 8944−8951.

(32) Liu, Y.-T.; Luo, X.-F.; Lee, Y.-Y.; Chen, I.-C. Investigating the Metal-Enhanced Fluorescence on Fluorescein by Silica Core-Shell Gold Nanoparticles Using Time-Resolved Fluorescence Spectroscopy. *Dyes Pigm.* **2021**, *190*, 109263.

(33) Asselin, J.; Roy, C.; Boudreau, D.; Messaddeq, Y.; Bouchared, R.; Mathieu, P. Supported Core-Shell Nanobiosensors for Quantitative Fluorescence Imaging of Extracellular PH. *Chem. Commun.* **2014**, *50*, 13746−13749.

(34) Asselin, J.; Lambert, M. P.; Fontaine, N.; Boudreau, D. A Ratiometric Nanoarchitecture for the Simultaneous Detection of PH and Halide Ions Using UV Plasmon-Enhanced Fluorescence. *Chem. Commun.* **2017**, *53*, 755−758.

(35) Tovmachenko, O. G.; Graf, C.; van den Heuvel, D. J.; van Blaaderen, A.; Gerritsen, H. C. Fluorescence Enhancement by Metal-Core/Silica-Shell Nanoparticles. *Adv. Mater.* **2006**, *18*, 91−95.

(36) Gashti, M. P.; Asselin, J.; Barbeau, J.; Boudreau, D.; Greener, J. A Microfluidic Platform with PH Imaging for Chemical and Hydrodynamic Stimulation of Intact Oral Biofilms. *Lab Chip* **2016**, *16*, 1412−1419.

(37) Fontaine, N.; Picard-Lafond, A.; Asselin, J.; Boudreau, D. Thinking Outside the Shell: Novel Sensors Designed from Plasmon-Enhanced Fluorescent Concentric Nanoparticles. *Analyst* **2020**, *145*, 5965−5980.

(38) Liu, H.-Y.; Zhao, M.; Qiao, Q.-L.; Lang, H.-J.; Xu, J.-Z.; Xu, Z.-C. Fluorescein-Derived Fluorescent Probe for Cellular Hydrogen Sulfide Imaging. *Chin. Chem. Lett.* **2014**, *25*, 1060−1064.

(39) Choi, M. G.; Cha, S.; Park, J. E.; Lee, H.; Jeon, H. L.; Chang, S.-K. Selective Perborate Signaling by Deprotection of Fluorescein and Resorufin Acetates. *Org. Lett.* **2010**, *12*, 1468−1471.

(40) Anifowose, A. J.; Takeda, K.; Sakugawa, H. Novel Fluorometric Method for the Determination of Production Rate and Steady-State Concentration of Photochemically Generated Superoxide Radical in Seawater Using 3′,6′-(Diphenylphosphinyl)Fluorescein. *Anal. Chem.* **2015**, *87*, 11998−12005.

(41) Lu, X.; Chen, Z.; Dong, X.; Zhao, W. Water-Soluble Fluorescent Probe with Dual Mitochondria/Lysosome Targetability for Selective Superoxide Detection in Live Cells and in Zebrafish Embryos. *ACS Sens.* **2018**, *3*, 59−64.

(42) Miller, E. W.; Albers, A. E.; Pralle, A.; Isacoff, E. Y.; Chang, C. J. Boronate-Based Fluorescent Probes for Imaging Cellular Hydrogen Peroxide. *J. Am. Chem. Soc.* **2005**, *127*, 16652−16659.

(43) Picard-Lafond, A.; Larivière, D.; Boudreau, D. Revealing the Hydrolysis Mechanism of a Hg2+-Reactive Fluorescein Probe: Novel Insights on Thionocarbonated Dyes. *ACS Omega* **2020**, *5*, 701−711.

(44) Sam, B.; George, L.; Varghese, A. Fluorescein Based Fluorescence Sensors for the Selective Sensing of Various Analytes. *J. Fluoresc.* **2021**, *31*, 1251−1276.

(45) Coelho-Souza, S. A.; Guimarães, J. R. D.; Mauro, J. B. N.; Miranda, M. R.; Azevedo, S. M. F. O. Mercury Methylation and Bacterial Activity Associated to Tropical Phytoplankton. *Sci. Total Environ.* **2006**, *364*, 188−199.

(46) Clarkson, T. W.; Magos, L. The Toxicology of Mercury and Its Chemical Compounds. *Crit. Rev. Toxicol.* **2006**, *36*, 609−662.

(47) World Health Organization. *Guidelines for Drinking-Water Quality*, 3rd ed.; World Health Organization: Geneva, 2004.

(48) Palmer, C. D.; Lewis, M. E.; Geraghty, C. M.; Barbosa, F.; Parsons, P. J. Determination of Lead, Cadmium and Mercury in Blood for Assessment of Environmental Exposure: A Comparison between Inductively Coupled Plasma-Mass Spectrometry and Atomic Absorption Spectrometry. *Spectrochim. Acta, Part B* **2006**, *61*, 980−990.

(49) Nolan, E. M.; Lippard, S. J. Tools and Tactics for the Optical Detection of Mercuric Ion. *Chem. Rev.* **2008**, *108*, 3443−3480.

(50) Aragay, G.; Pons, J.; Merkoçi, A. Recent Trends in Macro-, Micro-, and Nanomaterial-Based Tools and Strategies for Heavy-Metal Detection. *Chem. Rev.* **2011**, *111*, 3433−3458.

(51) Saleem, M.; Lee, K. H. Optical Sensor: A Promising Strategy for Environmental and Biomedical Monitoring of Ionic Species. *RSC Adv.* **2015**, *5*, 72150−72287.

(52) Kim, H. N.; Ren, W. X.; Kim, J. S.; Yoon, J. Fluorescent and Colorimetric Sensors for Detection of Lead, Cadmium, and Mercury Ions. *Chem. Soc. Rev.* **2012**, *41*, 3210−3244.

(53) Chen, G.; Guo, Z.; Zeng, G.; Tang, L. Fluorescent and Colorimetric Sensors for Environmental Mercury Detection. *Analyst* **2015**, *140*, 5400−5443.

(54) Samanta, T.; Shunmugam, R. Colorimetric and Fluorometric Probes for the Optical Detection of Environmental Hg(II) and As(III) Ions. *Mater. Adv.* **2021**, *2*, 64−95.

(55) Udhayakumari, D. Review on Fluorescent Sensors-Based Environmentally Related Toxic Mercury Ion Detection. *J. Inclusion Phenom. Macrocyclic Chem.* **2022**, *102*, 451−476.

(56) Wang, Y.; Zhang, L.; Han, X.; Zhang, L.; Wang, X.; Chen, L. Fluorescent Probe for Mercury Ion Imaging Analysis: Strategies and Applications. *Chem. Eng. J.* **2021**, *406*, No. 127166.

(57) Yuan, Z. H.; Yang, Y. S.; Lv, P. C.; Zhu, H. L. Recent Progress in Small-Molecule Fluorescent Probes for Detecting Mercury Ions. *Crit. Rev. Anal. Chem.* **2022**, *52*, 250−274.

(58) Cheng, Z.; Li, G.; Liu, M. A Metal-Enhanced Fluorescence Sensing Platform Based on New Mercapto Rhodamine Derivatives for Reversible Hg2+ Detection. *J. Hazard. Mater.* **2015**, *287*, 402−411.

(59) Cheng, Z.; Li, G.; Liu, M. Metal-Enhanced Fluorescence Effect of Ag and Au Nanoparticles Modified with Rhodamine Derivative in Detecting Hg2+. *Sens. Actuators, B* **2015**, *212*, 495−504.

(60) Kraithong, S.; Sirirak, J.; Soisuwan, K.; Wanichacheva, N.; Swanglap, P. Enhancing Sensitivity of Novel Hg2+ Fluorescent Sensor via Plasmonic Enhancement of Silver Nanoparticles. *Sens. Actuators, B* **2018**, *258*, 694−703.

(61) Kraithong, S.; Chailek, N.; Sirirak, J.; Suwatpipat, K.; Wanichacheva, N.; Swanglap, P. Improving Sensitivity of a New Hg2+-Selective Fluorescent Sensor by Silver Nanoparticles via Plasmonic Enhancement. *J. Photochem. Photobiol., A* **2021**, *407*, 113064.

(62) Lin, H. H.; Chen, I. C. Study of the Interaction between Gold Nanoparticles and Rose Bengal Fluorophores with Silica Spacers by Time-Resolved Fluorescence Spectroscopy. *J. Phys. Chem. C* **2015**, *119*, 26663−26671.

(63) Chhabra, R.; Sharma, J.; Wang, H.; Zou, S.; Lin, S.; Yan, H.; Lindsay, S.; Liu, Y. Distance-Dependent Interactions between Gold Nanoparticles and Fluorescent Molecules with DNA as Tunable Spacers. *Nanotechnology* **2009**, *20*, No. 485201.

(64) Malicka, J.; Gryczynski, I.; Gryczynski, Z.; Lakowicz, J. R. Effects of Fluorophore-to-Silver Distance on the Emission of Cyanine-Dye-Labeled Oligonucleotides. *Anal. Biochem.* **2003**, *315*, 57−66.

(65) Pang, Y.; Rong, Z.; Xiao, R.; Wang, S. "Turn on" and Label-Free Core−shell Ag@SiO2 Nanoparticles-Based Metal-Enhanced Fluorescent (MEF) Aptasensor for Hg2+. *Sci. Rep.* **2015**, *5*, No. 9451.

(66) Riccò, R.; Nizzero, S.; Penna, E.; Meneghello, A.; Cretaio, E.; Enrichi, F. Ultra-Small Dye-Doped Silica Nanoparticles via Modified Sol-Gel Technique. *J. Nanoparticle Res.* **2018**, *20*, No. 117.

(67) Duan, Q.; Zhu, H.; Liu, C.; Yuan, R.; Fang, Z.; Wang, Z.; Jia, P.; Li, Z.; Sheng, W.; Zhu, B. A Carbonothioate-Based Far-Red Fluorescent Probe for the Specific Detection of Mercury Ions in Living Cells and Zebrafish. *Analyst* **2019**, *144*, 1426−1432.

(68) Li, Q.; Hu, Y.; Hou, H.-N.; Yang, W.-N.; Hu, S.-L. A New Coumarin-Carbonothioate-Based Turn-on Fluorescent Chemodosimeter for Selective Detection of Hg2+. *Inorg. Chim. Acta* **2018**, *471*, 705−708.

(69) Mahouche-Chergui, S.; Grohens, Y.; Balnois, E.; Lebeau, B.; Scudeller, Y. Adhesion of Silica Particles on Thin Polymer Films Model of Flax Cell Wall. *Mater. Sci. Appl.* **2014**, *05*, 953−965.

(70) Martin, M. M.; Lindqvist, L. The PH Dependence of Fluorescein Fluorescence. *J. Lumin.* **1975**, *10*, 381−390.

(71) Lopes, C. B.; Otero, M.; Lin, Z.; Silva, C. M.; Pereira, E.; Rocha, J.; Duarte, A. C. Effect of PH and Temperature on Hg2+ Water Decontamination Using ETS-4 Titanosilicate. *J. Hazard. Mater.* **2010**, *175*, 439−444.

(72) World Health Organization. *Silver and Silver Compounds: Environmental Aspects*; World Health Organization: Geneva, 2002.